Type-II Dirac point and extreme dispersion in one-dimensional plasmonic-dielectric crystals with off-axis propagation

Zhenzhen Liu,[1,2] Qiang Zhang,[1,2] Feifei Qin,[1,2] Dasen Zhang,[1,2] Xiangli Liu,[1,3] and Jun Jun Xiao[1,2,*]

[1]*Shenzhen Engineering Laboratory of Aerospace Detection and Imaging, Harbin Institute of Technology (Shenzhen), Shenzhen 518055, China*

[2]*College of Electronic and Information Engineering, Harbin Institute of Technology (Shenzhen), Shenzhen 518055, China*

[3]*Department of Materials Science and Engineering, Harbin Institute of Technology (Shenzhen), Shenzhen 518055, China*

(Received 19 November 2018; published 22 April 2019)

Dirac cones exhibit linear crossing dispersion, which results in extraordinary topological properties in the energy bands. When the dispersion around the Dirac points is tilted, type-II or type-III Dirac points are present, which lead to intriguing transport phenomena. With the off-axis wave vector, a two-dimensional (2D) momentum space for one-dimensional (1D) crystals can be constructed. In this work, we revealed that the band structure in the extended 2D momentum space of carefully designed 1D plasmonic-dielectric crystals can be tuned to be highly tilted, forming type-II Dirac cones. In particular, an approximately upright dispersion can be achieved, which is referred to as a class-II Dirac point. Gapless interface states occur across the interface between two connected lattices formed by two distinct inversion-symmetry-broken crystals (i.e., type A and type B). The tilt of the band structure has a crucial influence on the formation of interface states and their sensitivity to the period, which results from the extraordinary properties of the surface impedance in the bulk gap. More importantly, class-II Dirac points exhibit peculiar topological properties. The wavelength area is divided into two regions, each of which can only support interface states for one configuration, type-AB or type-BA connections. Our results show that type-II Dirac points, especially those that are class II, have an underlying impact on the surface impedance and determine the existence of interface states.

DOI: 10.1103/PhysRevA.99.043828

I. INTRODUCTION

Topologically nontrivial states of matter have attracted considerable attention since the discovery of topological insulators [1–6]. In particular, Dirac or Weyl semimetals have been the focus of intensive research because they exhibit linear crossing dispersion in reciprocal space, which produces many interesting phenomena [7–13]. The nodal degeneracy in Dirac semimetals is protected by time-reversal symmetry and certain spatial symmetries. These ideas have been extended to classical systems, such as acoustic, mechanical, polaritonic, and electromagnetic systems [14–20].

Dirac cones (DCs) have been classified into several categories depending on the tilting degree of the cone: type I with a point-like Fermi surface and type II with a conical-like Fermi surface [9,10,21–24]. Many studies have been conducted on these peculiar DCs. In particular, the spatiotemporal symmetries of the constituent structures characterize the bulk bands and their topological properties. Breaking the time-reversal symmetry may lead to the quantum Hall effect due to the absence of counterpropagating states [25–28], while breaking certain spatial symmetries gives rise to quantum spin Hall effects [29,30] or valley Hall effects [24,31–33]. In these situations, the Berry curvature plays a crucial role in characterizing the topological properties. For spin Hall effects, the Chern number of the gapped bands becomes nontrivial, which is obtained by the integral of the Berry curvature in the Brillouin zone (BZ). For valley Hall effects, the Chern number for each band is unchanged, but the Berry curvatures in the opposite reciprocal regions have opposite signs, which is responsible for the emergence of interface states.

In a one-dimensional (1D) periodic system, only an intrinsic Bloch wave vector is available. With carefully designed parameters, the linear crossing bands can form in 1D momentum space, where a Dirac point (DP) emerges. Furthermore, off-axis propagation can extend the DC into two-dimensional (2D) space. In such a 2D reciprocal space, the degree of the band tilt of DCs can be tuned to be largely high. In particular, a DC with an upright dispersion, referred to as class II, can be constructed in the extended 2D space. To characterize the topological properties, surface impedance serves as an alternative metric to investigate the existence of topologically protected interface states [34,35].

In this work, we used 1D plasmonic-dielectric crystals to create type-II, and even class-II DCs in reciprocal space with an off-axis wave vector. The intrinsic geometrical dimension was used to tune the degree of tilt, especially the slope of one energy band. Beyond a certain threshold, vertical dispersion emerged, which could significantly affect the distribution of surface impedance and the resultant interface states between the opposite inversion-broken lattices (labeled as type A and type B). The distribution of the surface impedance in the common gap was observed to be monotonic. In particular, a differential distribution, which was a piecewise function, ensured the crossing of the surface impedance between two different inversion-broken types across the interface, i.e., the existence of topologically protected interface states. More

*eiexiao@hit.edu.cn

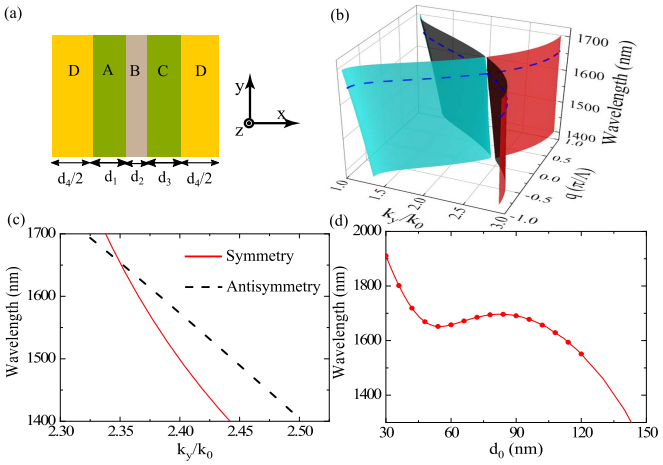

FIG. 1. (a) Schematic diagram of the multilayered lattices composed of four alternating stacks. (b) The dispersion of an inversion-symmetric crystal with $d_1 = d_3 = d_0 = 52$ nm. (c) The dispersion of the symmetric and antisymmetric states on plane $q = 0$ of (b). (d) The trajectory of the DPs over the (λ, d_0) plane, where $d_2 = 8.5$ nm and $\Lambda = d_1 + d_2 + d_3 + d_4 = 308.5$ nm.

specifically, the vertical dispersion implies a peculiar topological configuration: The interface states only existed in either type-BA or type-AB connections based on the selected wavelength.

II. DISPERSION RELATION AND EFFECTIVE HAMILTONIAN AROUND DIRAC POINT

Figure 1(a) schematically shows the inversion-symmetric unit cell with multilayered stacks: Two identical dielectric waveguides, layers A and C (both silica with a refractive index $n_1 = n_3 = 1.44$), are connected by dielectric layer D (silicon with $n_4 = 3.48$) and metal layer B (silver with Drude permittivity ε_2 [36]). The fundamental bands are ascribed to the coupling of modes supported in layers A and C. Note that a DP is preserved if the coupling strengths via the plasmonic (layer B) and dielectric (layer D) layers have opposite signs [37,38]. Herein, we use the transfer matrix method (TMM) [34,39] to obtain the transverse magnetic (TM) dispersion relation of such a plasmonic-dielectric crystal. The corresponding TM dispersion relation is as follows (see Appendix A):

$$\begin{aligned}\frac{4\cos(q\Lambda)}{\Xi} = 4 &+ \left(\tau_{24} + \frac{1}{\tau_{24}} - \tau_{21}\tau_{34} - \frac{1}{\tau_{21}\tau_{34}}\right) \\ &\times \frac{\tan\kappa_2 \tan\kappa_4 \cos(\kappa_1 - \kappa_3)}{\cos(\kappa_1 + \kappa_3)} \\ &- 2(\tau_{21} + \tau_{32})\tan\kappa_2 \tan(\kappa_1 + \kappa_3) \\ &- 2(\tau_{14} + \tau_{43})\tan\kappa_4 \tan(\kappa_1 + \kappa_3) \\ &- \left(\tau_{24} + \frac{1}{\tau_{24}} + \tau_{21}\tau_{34} + \frac{1}{\tau_{21}\tau_{34}}\right)\tan\kappa_2 \tan\kappa_4, \end{aligned} \tag{1}$$

where q represents the on-axis wave vector along the x direction; k_y denotes the off-axis wave vector along the y direction; $\Lambda = d_1 + d_2 + d_3 + d_4$ is the width of the unit cell; $k_0 = 2\pi/\lambda_0$ with a vacuum wavelength λ_0; $\Xi = \cos\kappa_2 \cos\kappa_4 \cos(\kappa_1 + \kappa_3)$; $\kappa_m = k_m d_m$; $\tau_{mn} = \varepsilon_m k_n/\varepsilon_n k_m$; and $k_m = \sqrt{k_0^2\varepsilon_m - k_y^2}$, with $m = 1, 2, 3$, and 4 corresponding to layers A, B, C, and D in Fig. 1(a), respectively. Equation (1) describes the dispersion relation between the frequency $\omega = k_0 c$ (wavelength $\lambda_0 = 2\pi/k_0$), the on-axis wave vector q, and the off-axis wave vector k_y. In this study, we set $d_2 = 8.5$ nm and $\Lambda = 308.5$ nm. For simplicity, we ignore the loss of metal in the following calculations.

Figure 1(b) shows the band structure of a specific crystal with $d_1 = d_3 = d_0 = 52$ nm. Here, d_0 in particular is used to characterize the inversion-symmetric structure with equal d_1 and d_3. A nodal degeneracy appears with a tilted conical dispersion, leading to a peculiar crossing dispersion in the constant-energy plane [see the dashed line in Fig. 1(b)] [9,24]. A phase transition occurs when the parameter d_0 crosses the DP, as shown in Fig. 1(c). The symmetric and antisymmetric states simultaneously exchange their positions [40]. The field distribution can be obtained by the TMM (see Appendix B). DPs in this inversion-symmetric crystal are robust due to their emergence with an allowed d_0, as illustrated in Fig. 1(d). The role of d_0 is to modify the position of the DPs and simultaneously tune the tilt degree of the type-II DCs. We emphasize that the tilted dispersions are critical for controlling and modulating the topological protected interface states, which will be discussed in more detail.

As reported previously, the Hamiltonian near a DP can be effectively written as $H = (v_{0x}k_x + v_{0y}k_y)\sigma_0 + v_x k_x \sigma_x + v_y k_y \sigma_y$ [21,24], where v_{0x}, v_{0y}, v_x, and v_y are the effective velocities and σ_0 and σ_i are the identity matrix and Pauli matrices, respectively. If the tilt parameter of the aforementioned Hamiltonian, i.e., $\mu = \sqrt{(v_{0x}/v_x)^2 + (v_{0y}/v_y)^2}$, is greater than unity, it is for a type-II DP. To better understand the topological properties of the DPs in our model, we write the effective Hamiltonian around the DP in Fig. 1(b) as (see Appendix C) follows:

$$H_{\text{eff}} = v_{0y}\Delta k_y \sigma_0 + v_x \Delta k_y \sigma_x + v_y \Delta k_y \sigma_y + v_z \Delta q \sigma_z, \tag{2}$$

where $(\Delta q, \Delta k_y)$ is the wave-vector deviation with respect to that of the DP. In the form of Eq. (2), the tilt parameter becomes $\mu = v_{0y}/\sqrt{v_x^2 + v_y^2}$, where $\mu > 1$ is also satisfied (see Appendix C), which ensures that this is a type-II DC in Fig. 1(b).

III. DISPERSION RELATION, SURFACE IMPEDANCE, AND THE RESULTANT INTERFACE STATES

Generally, DPs are protected by the product of time-reversal and inversion symmetry. The inversion symmetry of the above-mentioned plasmonic-dielectric crystal is broken by setting unequal thicknesses of layers A and C, i.e., $d_1 \neq d_3$ ($d_1 = d_0 + d_a$, $d_3 = d_0 - d_a$), as sketched in Fig. 2(a). We define type A as the inversion-broken crystal with $d_a > 0$ and type B as the inversion-broken crystal with $d_a < 0$. As the inversion symmetry is broken, the DP is lifted. For example, by setting $d_0 = 52$ nm and $d_a = \pm 10$ nm, a gapped band structure appears, as shown in Fig. 2(b). The Zak phase of the 1D inversion-broken crystal ($d_a \neq 0$) cannot be quantized as 0 or π [34,40]. As the nodal degeneracy is at the center

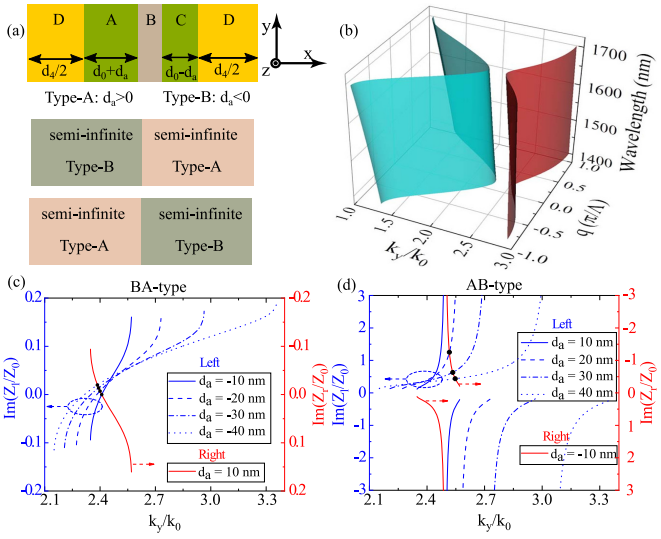

FIG. 2. (a) Schematic plots of the inversion-broken lattices: type A and type B, connected in BA- and AB-type configurations. (b) The band structure of the inversion-broken crystal with $d_a = \pm 10$ nm for $d_0 = 52$ nm. (c), (d) Im(Z_l) for the left semi-infinite crystal (marked in blue) and Im(Z_r) for the right semi-infinite crystal (marked in red) as a function of k_y for wavelength $\lambda = 1450$ nm. Here $Z_0 = 376.73\ \Omega$ is the vacuum impedance. The crossing points of the red and blue lines in (c), (d) indicate that $\mathrm{Im}(Z_l) + \mathrm{Im}(Z_r) = 0$.

of the on-axis wave vector $q = 0$, the opposite sign of the Berry curvature for $k_y > 0$ and $k_y < 0$ accounts for the valley Hall effect for inversion-broken lattices connected in the y direction [24]. However, the semi-infinite type-A and type-B crystals are connected in the x direction, as shown in Fig. 2(a). Therefore, the Berry curvature can no longer be responsible for the valley Hall effect [24].

To investigate the topologically protected interface states across the interface, surface impedance serves as an alternative tool. The surface impedance for the right semi-infinite crystal can be directly derived by the TMM as $Z_r = E_y/H_z$ [34]. The opposite sign of the surface impedance in the common gap guarantees the existence of a topologically protected interface state [34,35]:

$$Z_l + Z_r = 0, \tag{3}$$

where Z_l (Z_r) is the surface impedance of the medium on the left-hand side (right-hand side) of an interface. There are two distinct sequences for the connection of the type-A and type-B lattices, namely, the BA-type and AB-type configurations, as shown in Fig. 2(a). We emphasize that the surface impedance for the type-A crystal fully differs from that of type B, which creates the intriguing possibility of engineering topologically protected interface states.

Figure 2(b) shows the gapped band structure due to the presence of nonzero d_a. Inside the gap, the surface impedance is purely imaginary. Figure 2(c) [2(d)] plots the variation of Im(Z_r) and Im(Z_l) of the BA-type (AB-type) configurations for a fixed wavelength, $\lambda = 1450$ nm, as a function of k_y. For the connection of the BA-type configuration, the Im(Z) of the right type-A and left type-B crystals varies monotonically as k_y increases [see the red and blue curves in Fig. 2(c), respectively]. Due to the opposite signs between Im(Z_l) and Im(Z_r) and their monotonicity in Fig. 2(c), the intersection points establish the zero surface impedance condition of $\mathrm{Im}(Z_l) + \mathrm{Im}(Z_r) = 0$ and support only one interface state at one particular pair (k_y, q) [35]. The surface impedances are identical if the magnitude of d_a is the same on both sides of the interface but signs of d_a are opposite. Thus, the requirement of $\mathrm{Im}(Z_l) + \mathrm{Im}(Z_r) = 0$ can be guaranteed only if Im(Z_r) vanishes in the gap. Increasing d_a would enhance the inversion-breaking degree, resulting in the expansion of the gap region. Hence, a monotonic variation of surface impedance can be ensured to cross the surface impedance with the augmented $|d_a|$ [see the intersection between the red line and blue dashed (dot-dashed and dotted) lines in Fig. 2(c)]. As such, we can conclude that the interface states can always exist in the BA-type configuration.

For the connection of the AB-type configuration, the behavior is completely different. For the left type-A and right type-B crystals, Im(Z) is distributed like a piecewise function. In the positive region, Im(Z) tends to infinity, while in the negative region, it increases from negative infinity [see red and blue lines in Fig. 2(d), respectively]. For this kind of AB-type connection, the right and left surface impedances cannot cancel out for the same $|d_a|$ [see the red and blue solid lines in Fig. 2(d)]. Similar to the aforementioned BA-type connection, the increase in d_a can broaden the gap region and ensure that an intersection occurs, as shown in Fig. 2(d) [i.e., $\mathrm{Im}(Z_l) + \mathrm{Im}(Z_r) = 0$], between different crystals with unequal values of $|d_a|$. For a more intuitive description, we visualize the distribution of the surface impedance as a power function of the form $a(k_y - k_{y0})^b$, with a positive power $b = 2n + 1$ for the aforementioned BA-type configuration and negative power $b = -(2n + 1)$ for the AB-type configuration, where n is a positive integer. As the d_a of the left type A varies, the corresponding k_y where $\mathrm{Im}(Z_l) + \mathrm{Im}(Z_r) = 0$ can also be satisfied (see the intersection points between the red solid and blue dashed [dot-dashed and dotted) lines in Fig. 2(d)].

Referring to Fig. 1(d), the trajectory of the DP continuously spans the allowed d_0. For an arbitrary d_0 between 30 and 150 nm, the DCs are of type II. In addition, the slope of the symmetry states at $q = 0$ becomes steeper with increased d_0. Figure 3 shows the results for crystals with an enlarged $d_0 = 116.37$ nm. Apparently, the symmetric state dispersion curve in Fig. 3(b) is approximately vertical. All of these factors have significant effects on the distribution of the surface impedance. The dependences of Im(Z) on k_y in Figs. 3(c) and 3(d) are similar to those in Figs. 2(c) and 2(d). However, all of the curves for the BA-type configuration shown in Fig. 3(c) only extend slightly into the negative region. In this case, the blue and red curves can still intersect at their appropriate k_y. However, this requires more rigorous constraints: Both sides across the interface should possess sufficient periodicity to mimic the semi-infinite property. For the AB-type connection, the requirement of $\mathrm{Im}(Z_l) + \mathrm{Im}(Z_r) = 0$ is satisfied in the region of the surface impedance extending to infinity. As such, the resultant interface state is less sensitive to the size of the crystal, which is similar to the behavior in Fig. 2(d).

As d_0 continues to increase, the slope of the symmetric state becomes nearly vertical upon further increasing d_0 to

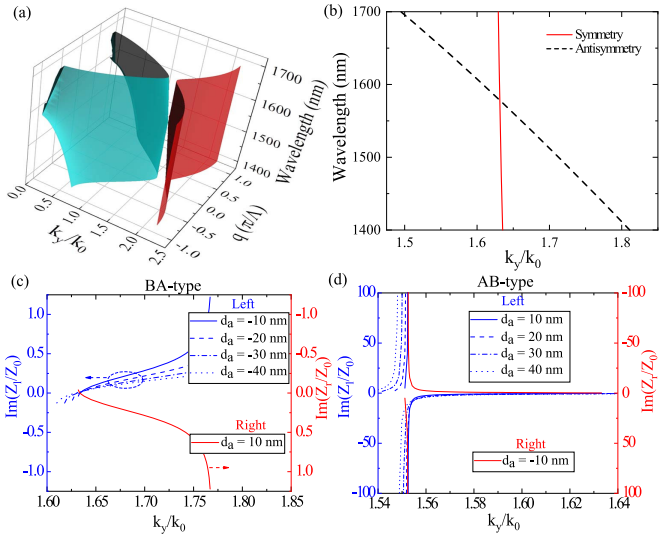

FIG. 3. (a) Band structure of the inversion-symmetry-broken crystal for $d_0 = 116.37$ nm. (b) Band structure of symmetric and antisymmetric states for $q = 0$ in (a). (c), (d) Im(Z_l) for the left semi-infinite crystal (blue curves) and Im(Z_r) for the right semi-infinite crystal (red curve) as a function of k_y for $\lambda = 1450$ nm.

140 nm [see the red line in Fig. 4(b)]. In this case, the gap can be divided into two parts, and they can be classified according to the value of the wavelength: region I below the DP (approximately, 1345 nm) and region II above the DP. In region I, the variation of Im(Z) for the type-A crystal [solid black and dashed red lines in Fig. 4(c)] monotonically increases in the positive range, and that for the type-B crystal [solid black and dashed red lines in Fig. 4(d)] is a power function with the form $a(k_y - k_{y0})^b$, with $b = -(2n + 1)$. However, when the wavelength lies in region II, the variations of Im(Z) for

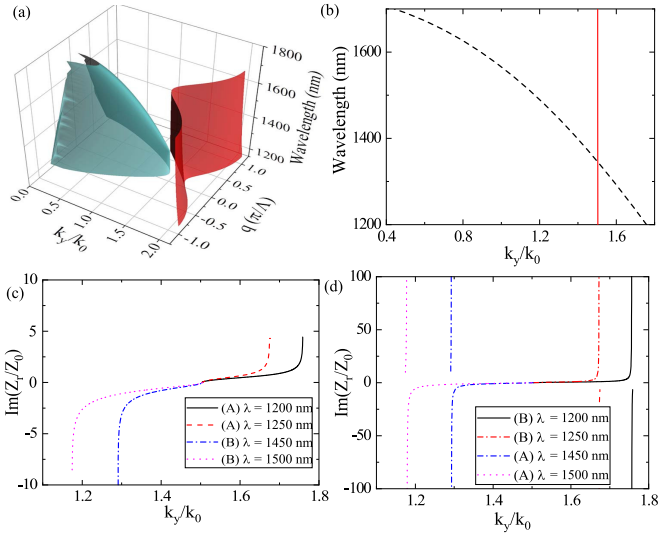

FIG. 4. (a) Band structure of the inversion-symmetry-broken crystal for $d_0 = 140$ nm. (b) Band structure of symmetric and antisymmetric states for $q = 0$ in (a). (c), (d) Im(Z_r) for the right semi-infinite crystal (red curves) as a function of k_y for four selected wavelengths on both sides of the DP in (b).

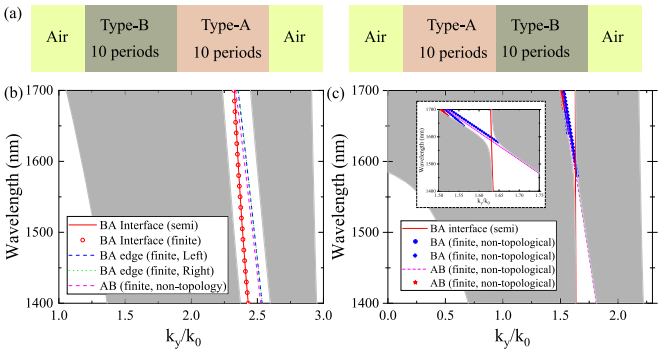

FIG. 5. (a) Finite lattice configuration of type BA and type AB surrounded by air. The trajectories of the interface states in the gap regions for (b) $d_0 = 52$ nm and (c) $d_0 = 116.37$ nm crystal for type A ($d_a = 10$ nm) and type B ($d_a = -10$ nm), respectively. The gray region indicates the projection of the bulk bands.

types A and B are exchanged: Im(Z) for type B [dot-dash blue and dotted pink line in Fig. 4(c)] becomes monotonic in the negative range, while Im(Z) for type A [dot-dash blue and dotted pink lines in Fig. 4(d)] becomes power functions. Thus, the connection between crystals with monotonically increasing Im(Z) cannot support the topologically protected interface states, while the power-function-like Im(Z) with a negative index can protect the formation of interface states between the crystals with different values of $|d_a|$. It is then straightforward to find the interface state for the AB-type configuration located in region I. On the contrary, the interface state for the BA-type configuration is in region II. For more details, see Appendix D. This extraordinary type-II DP is classified as class II, distinguished from the former cases shown in Figs. 2 and 3.

Now we exemplify the distribution of interface states for the inversion-broken crystal with the same $|d_a| = 10$ nm for the right and left lattices. Figure 5(a) schematically illustrates the constructed crystal configuration. As we revealed in the analysis above (see Figs. 2 and 3), the semi-infinite crystal connection for the BA type guarantees the existence of a topological interface state, while this is not the case for the AB type [see the red solid line in Figs. 5(b) and 5(c), respectively]. Extended to the connection between type A and type B with finite cells (ten periods on both sides of the interface), the topologically protected interface states for type-BA connections can exist for $d_0 = 52$ nm [see red circles in Fig. 5(b)] and do not exist for $d_0 = 116.37$ nm [see Fig. 5(c)]. Indeed, the interface states can reappear for $d_0 = 116.37$ nm if we increase the sizes of the lattices, for example, to 20 periods. This is due to the small leap over zero mentioned above [refer to Fig. 3(c)]. In addition, there are interface states that are nontopological and some edge states supported on the interfaces between the lattices and background air [see the blue and green dashed lines in Fig. 5(b)]. Similarly, the topologically protected interface states for the type-A and type-B connections with different degrees of inversion breaking (i.e., different values of $|d_a|$) can also be observed and verified in a similar way (results are not shown here). We emphasize that the unique properties of class-II DPs in this

1D crystal are of vital significance for the existence of the topologically protected interface states.

A few additional comments are needed. First, loss could be a crucial issue for the system. However, for our considered wavelength region around $\lambda = 1550$ nm, the imaginary parts of the silver dielectric function are two orders of magnitude smaller than the real parts. Furthermore, the filling factor of the silver slices is around 1/50. As a result, the complex band structure exhibits a real k_y that is three orders of magnitude larger than the imaginary k_y, namely, $\mathrm{Re}(k_y) \sim 10^3 \mathrm{Im}(k_y)$, and the gap around the degeneracy point remains open when the loss is accounted for in the inversion-symmetry-broken crystals. The corresponding information is presented in Appendix E. Furthermore, increasing the inversion-breaking degree can enlarge the gaps, where the absorption effects of smearing out the gap can be avoided.

IV. CONCLUSION

In conclusion, we explored Dirac points in the extended wave-vector space (on axis and off axis) of 1D plasmonic-dielectric crystals. The tilted type-II Dirac cone, especially a nearly vertical band, has significant effects on the formation of topologically protected interface states. This is because the tilt degree of the Dirac cone greatly influences the features of the gap, which are reflected in the profiles of the surface impedance. The existence or lack of topological interface states can be used to realize frequency-dependent optical information transportation and optical switches. This idea has the potential to extend to other platforms, e.g., metasurfaces, plasmonics, and photonics. Besides the Bloch wave vector, the off-axis wave vector and the notion of the synthetic dimension can further enrich the topological physics in lower-dimensional systems. More importantly, it may be possible to engineer on-site potential profiles in 2D electron systems, e.g., single-layer or few-layer graphene [41]; van der Waals 2D materials, such as transition metal dichalcogenides [42]; or moiré superlattices [43], providing an additional degree of freedom and allowing the exploration of the electron surface states with the aid of the synthetic space.

ACKNOWLEDGMENTS

This work was supported by Shenzhen Municipal Science and Technology Plan (Grants No. JCYJ20180306172003963 and No. JCYJ20170811154119292), NSF of Guangdong Province (Grant No. 2015A030313748), and NSFC (Grant No. 11672090).

APPENDIX A: DERIVATION OF THE DISPERSION RELATION

The TMM was utilized to obtain the band structure of the four multilayered stacks as shown in Fig. 1. The relation between the incident and scattering waves can be characterized by a 2×2 matrix [34,39]. Thus, the transfer matrix at the interface from layer m to layer n is as follows:

$$\mathbf{M}_{mn} = \frac{1}{2}\begin{bmatrix} \frac{1+\tau_{mn}}{\tau_{mn}} & \frac{-1+\tau_{mn}}{\tau_{mn}} \\ \frac{-1+\tau_{mn}}{\tau_{mn}} & \frac{1+\tau_{mn}}{\tau_{mn}} \end{bmatrix}, \tag{A1}$$

where $\tau_{mn} = \varepsilon_m k_n / \varepsilon_n k_m$ and $k_m = \sqrt{k_0^2 \varepsilon_m - k_y^2}$, with $m = 1,2,3$, and 4 corresponding to layers A, B, C, and D, respectively.

The propagation matrix in layer m is described by

$$\mathbf{M}_m = \begin{bmatrix} e^{ik_m d_m} & 0 \\ 0 & e^{-ik_m d_m} \end{bmatrix}, \tag{A2}$$

where d_m is the thickness of layer m. The transfer matrix of a unit cell is

$$\mathbf{M} = \mathbf{M}_{41}\mathbf{M}_4\mathbf{M}_{34}\mathbf{M}_3\mathbf{M}_{23}\mathbf{M}_2\mathbf{M}_{12}\mathbf{M}_1. \tag{A3}$$

According to the Bloch theorem, the dispersion relation [39] can be expressed as

$$\cos(q\Lambda) = \tfrac{1}{2}(M_{11} + M_{22}), \tag{A4}$$

where q is the Bloch wave vector, Λ the thickness of the lattice supercell, and M_{11} and M_{22} the diagonal elements of $\mathbf{M}$ in Eq. (A3). To obtain a definite expression, we decompose Eq. (A3) into two parts, each of which consists of two layers.

$$\mathbf{M'}_{12} = \mathbf{M}_{23}\mathbf{M}_2\mathbf{M}_{12}\mathbf{M}_1 = \begin{bmatrix} m_{11} & m_{12} \\ m_{21} & m_{22} \end{bmatrix}, \tag{A5}$$

$$\mathbf{M'}_{34} = \mathbf{M}_{41}\mathbf{M}_4\mathbf{M}_{34}\mathbf{M}_3 = \begin{bmatrix} m'_{11} & m'_{12} \\ m'_{21} & m'_{22} \end{bmatrix}. \tag{A6}$$

The elements of these two matrices are as follows:

$$m_{11} = \frac{e^{i\kappa_1}}{2}[(\tau_{31}+1)\cos\kappa_2 + i(\tau_{32}+\tau_{21})\sin\kappa_2], \tag{A7}$$

$$m_{12} = \frac{e^{-i\kappa_1}}{2}[(-\tau_{31}+1)\cos\kappa_2 + i(\tau_{32}-\tau_{21})\sin\kappa_2], \tag{A8}$$

$$m_{21} = \frac{e^{i\kappa_1}}{2}[(-\tau_{31}+1)\cos\kappa_2 + i(-\tau_{32}+\tau_{21})\sin\kappa_2], \tag{A9}$$

$$m_{22} = \frac{e^{-i\kappa_1}}{2}[(\tau_{31}+1)\cos\kappa_2 - i(\tau_{32}+\tau_{21})\sin\kappa_2], \tag{A10}$$

$$m'_{11} = \frac{e^{i\kappa_3}}{2}[(\tau_{13}+1)\cos\kappa_4 + i(\tau_{43}+\tau_{14})\sin\kappa_4], \tag{A11}$$

$$m'_{12} = \frac{e^{-i\kappa_3}}{2}[(-\tau_{13}+1)\cos\kappa_4 + i(-\tau_{43}+\tau_{14})\sin\kappa_4], \tag{A12}$$

$$m'_{21} = \frac{e^{i\kappa_3}}{2}[(-\tau_{13}+1)\cos\kappa_4 + i(\tau_{43}-\tau_{14})\sin\kappa_4], \tag{A13}$$

$$m'_{22} = \frac{e^{-i\kappa_3}}{2}[(\tau_{13}+1)\cos\kappa_4 - i(\tau_{43}+\tau_{14})\sin\kappa_4], \tag{A14}$$

where $\tau_{mn} = \varepsilon_m k_n / \varepsilon_n k_m$. From Eqs. (A7)–(A14), we can further simplify the expression if the first and the third layers are identical, i.e., $\tau_{13} = 1$. In this case, Eq. (A4) becomes

$$\frac{4\cos(q\Lambda)}{\Xi} = 4 + \left(\tau_{24} + \frac{1}{\tau_{24}} - \tau_{21}\tau_{34} - \frac{1}{\tau_{21}\tau_{34}}\right) \times \frac{\tan\kappa_2 \tan\kappa_4 \cos(\kappa_1 - \kappa_3)}{\cos(\kappa_1 + \kappa_3)} - 2(\tau_{14} + \tau_{43})\tan\kappa_4 \tan(\kappa_1 + \kappa_3)$$

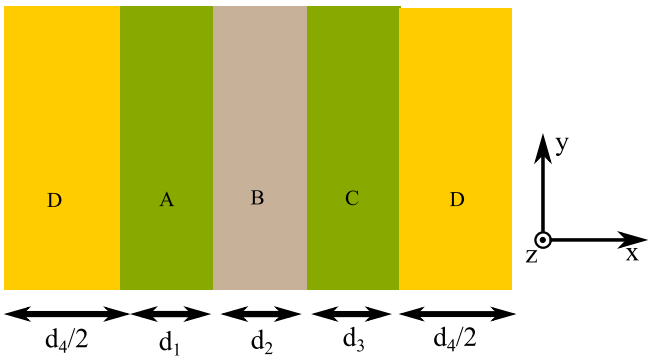

FIG. 6. Schematic diagram of the multilayered lattice composed of four alternating stacks. The origin of the supercell is fixed at the center of metal layer B.

$$-2(\tau_{21}+\tau_{32})\tan\kappa_2\tan(\kappa_1+\kappa_3) - \left(\tau_{24}+\frac{1}{\tau_{24}}+\tau_{21}\tau_{34}+\frac{1}{\tau_{21}\tau_{34}}\right)\tan\kappa_2\tan\kappa_4. \tag{A15}$$

APPENDIX B: BLOCH WAVE FUNCTION IN THE SUPERCELL AND ZAK PHASE CALCULATION

We choose the origin of the supercell to be at the center of metal layer B. The eigenvector of the transfer matrix of the supercell is $[M_{12}, \exp(iq\Lambda) - M_{11}]$, where M_{11} and M_{12} are the elements of the total transfer matrix shown in Fig. 6. The modal magnetic field (H_z) and electric field (E_y) along the x direction in the first layer are as follows [34]:

$$H_z(x) = M_{12}e^{ik_4(x+\Lambda/2)} + (e^{iq\Lambda} - M_{11})e^{-ik_4(x+\Lambda/2)}, \tag{B1}$$

$$E_y(x) = \frac{k_4}{\omega\varepsilon_4}[M_{12}e^{ik_4(x+\Lambda/2)} + (e^{iq\Lambda} - M_{11})e^{-ik_4(x+\Lambda/2)}], \tag{B2}$$

where M_{12} and $\exp(iq\Lambda) - M_{11}$ are, respectively, the coefficients of the forward and backward wave at the left port. After the wave reaches the next layer, layer A in Fig. 6, the coefficients of the forward and backward wave change to s_{12}, s_{11}, respectively. They can be directly obtained by

$$(s_{12}, s_{11})^T = \mathbf{M}_{41}\mathbf{M}'_4[M_{12}, \exp(iq\Lambda) - M_{11}]^T, \tag{B3}$$

where $\mathbf{M}'_4$ is the propagation matrix in the first layer with length $d_4/2$. The magnetic and electric fields in the second layer (Fig. 6) are

$$H_z(x) = s_{12}e^{ik_1(x+\Lambda/2-d_4/2)} + s_{11}e^{-ik_1(x+\Lambda/2-d_4/2)}, \tag{B4}$$

$$E_y(x) = \frac{k_1}{\omega\varepsilon_1}[s_{12}e^{ik_1(x+\Lambda/2-d_4/2)} + s_{11}e^{-ik_1(x+\Lambda/2-d_4/2)}]. \tag{B5}$$

Extending this treatment to the entire supercell, the eigenfield distribution can be obtained. Furthermore, with periodic gauge, the Zak phase of each band can be calculated by the Pancharatnam discrete approach [34]:

$$\theta_Z = i\int_{\mathrm{BZ}}\int_{\mathrm{unit}} u_q^*\partial_q u_q dx dq, \tag{B6}$$

where $u_q(x)$ is the Bloch wave function $H_{z,q}(x) = u_q(x)\exp(iqx)$ for the supercell of Fig. 6. The results are in accord with the symmetry distribution of the band edge states in the main text.

APPENDIX C: EFFECTIVE HAMILTONIAN AROUND THE DEGENERACY

To obtain the effective Hamiltonian, we begin from the entire transfer matrix of the unit cell, i.e., Eq. (A3). Note that the DPs in the inversion-symmetric system with $d_0 = 52$ nm are located at ($\lambda = 1654.3$ nm, $k_{y0} = 2.35k_0$). The effective Hamiltonian around this point can be obtained by the following procedure.

The eigenvalue formulation of this problem can be written as

$$(\mathbf{M} - e^{iq\Lambda})\begin{bmatrix}a_+\\a_-\end{bmatrix} = 0, \tag{C1}$$

where a_+ and a_- indicate the coefficients of the forward- and backward-propagating waves inside the first layer, respectively. We define the following coefficients,

$$(\Delta\lambda, \Delta q, \Delta k_y) = \left(\frac{\lambda-\lambda_0}{\lambda_s}, \frac{q-q_0}{\pi/\Lambda}, \frac{k_y-k_{y0}}{k_0}\right), \tag{C2}$$

where (d_0, q_0) indicates the position of the DP with propagation constants k_{y0} as shown in Fig. 1(e), and $q_0 = 0$ lies in the center of the Brillouin zone. Here $\lambda_s = 1500$ nm and $p = d_1 + d_3 + d_4$ denotes the thickness of the entire dielectric medium. Expanding $\mathbf{M}$ up to the first order with respect to $(\Delta d_1, \Delta d_2, \Delta k_y)$ around the DP, we have

$$\mathbf{M} = \begin{pmatrix} a_{11}+b_{11}\Delta\lambda+c_{11}\Delta k_y & a_{12}+b_{12}\Delta\lambda+c_{12}\Delta k_y \\ a_{21}+b_{21}\Delta\lambda+c_{21}\Delta k_y & a_{22}+b_{22}\Delta\lambda+c_{22}\Delta k_y \end{pmatrix} + O(\Delta\lambda^2, \Delta k_y^2). \tag{C3}$$

Considering only the first order, Eq. (C3) can be rewritten as

$$\begin{pmatrix} a_{11}+c_{11}\Delta k_y-1-j\Delta q & a_{12}+c_{12}\Delta k_y \\ a_{21}+c_{21}\Delta k_y & a_{22}+c_{21}\Delta k_y-1-j\Delta q \end{pmatrix}\begin{bmatrix}a_+\\a_-\end{bmatrix} = \Delta\lambda\begin{bmatrix}-b_{11} & -b_{12}\\ -b_{21} & -b_{22}\end{bmatrix}\begin{bmatrix}a_+\\a_-\end{bmatrix}. \tag{C4}$$

We denote the matrix on the left-hand side of Eq. (C4) by $\mathbf{T}$, and the matrix on the right-hand side by $\mathbf{V}$. The matrix $\mathbf{V}$ can be decomposed as $\mathbf{V} = \mathbf{U}\mathbf{D}\mathbf{U}^\dagger$. Equation (C4) can be rewritten as

$$\mathbf{D}^{-1/2}\mathbf{U}^\dagger\mathbf{T}\mathbf{U}\mathbf{D}^{-1/2}(\mathbf{D}^{1/2}\mathbf{U}^\dagger\mathbf{a}) = \Delta k_y(\mathbf{D}^{1/2}\mathbf{U}^\dagger\mathbf{a}). \tag{C5}$$

This can also be represented as

$$\mathbf{H}\mathbf{p} = \Delta\lambda\mathbf{p}, \tag{C6}$$

where $\mathbf{H}$ can be regarded as the Hamiltonian of the system near a random point.

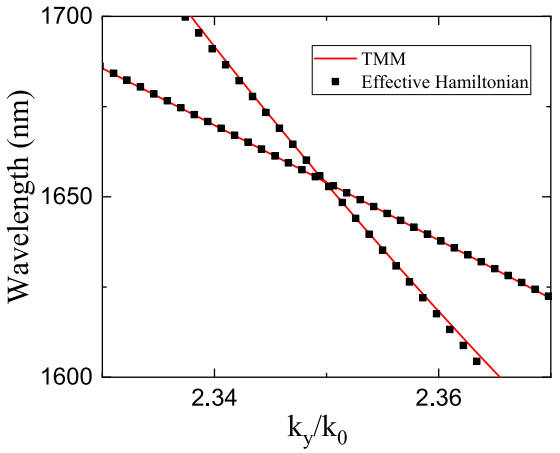

FIG. 7. Dispersions near the DPs. The lines are the rigorous theoretical results obtained by the TMM, and the black squares are the results from the effective Hamiltonian.

For the DP ($d_1 = d_2 = d_0 = 52$ nm, $\lambda = 1654.3$ nm, $k_y = 2.35k_0$), the Hamiltonian can be written as

$$H_{\text{eff}} = v_{0y}\Delta k_y \sigma_0 + v_x \Delta k_y \sigma_x + v_y \Delta k_y \sigma_y + v_z \Delta q \sigma_z, \quad \text{(C7)}$$

with $v_{0y} = -1.7539$, $v_x = -0.3358$, $v_y = -0.4382$, and $v_z = -1.7843$.

To verify the validity of the effective Hamiltonian, we plotted the dispersion along the three directions in Fig. 7. The results obtained by the TMM and the effective Hamiltonian agree very well near the degeneracy. The effective Hamiltonian for the other DPs in Fig. 1(d) can be obtained using a similar procedure.

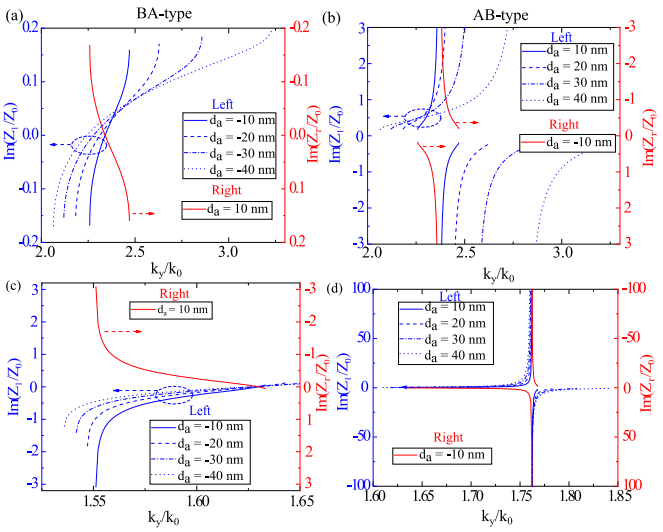

FIG. 8. The values of $\text{Im}(Z_l)$ for a left semi-infinite crystal (marked in blue) and $\text{Im}(Z_r)$ for a right semi-infinite crystal (marked in red) as a function of k_y for a fixed wavelength $\lambda = 1650$ nm with (a), (b) $d_0 = 52$ nm and (c), (d) $d_0 = 116.37$ nm.

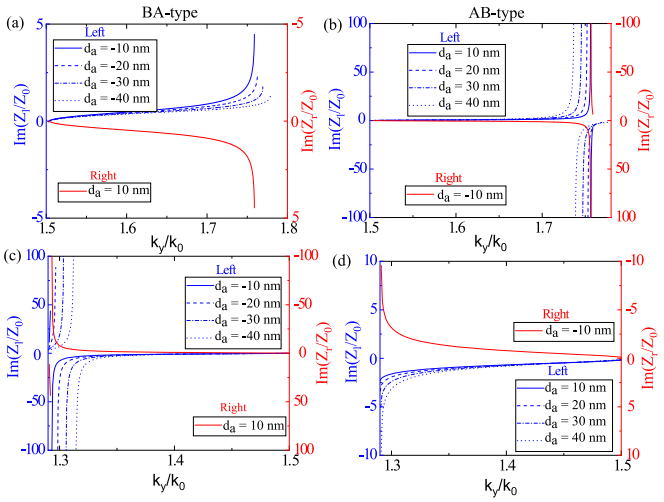

FIG. 9. The values of $\text{Im}(Z_l)$ for a left semi-infinite crystal (marked in blue) and $\text{Im}(Z_r)$ for a right semi-infinite crystal (marked in red) as a function of k_y for a fixed $d_0 = 140$ nm with (a), (b) $\lambda = 1200$ nm and (c), (d) $\lambda = 1450$ nm.

APPENDIX D: DISTRIBUTION OF SURFACE IMPEDANCE AT OTHER WAVELENGTHS

The variation of surface impedance at $\lambda = 1450$ nm is shown in Figs. 2 and 3. These figures characterize the consistence of the distribution of $\text{Im}(Z)$. We offer the distributions of $\text{Im}(Z)$ at wavelengths above the DP. Figure 8 shows the variation of $\text{Im}(Z)$ for the BA- and AB-type connections at $\lambda = 1650$ nm. The results are in accord with the main text.

To verify the different properties of the crystal with $d_0 = 140$ nm, we provide similar distribution of $\text{Im}(Z)$ at different wavelengths, as shown in Fig. 9. This is similar to the results in Figs. 3(c) and 3(d). However, a surprising transition occurs for the surface impedance between the BA- and AB-type connection.

In addition, to verify the efficiency of the prediction in Fig. 2(c), we implement the BA-type connection with finite

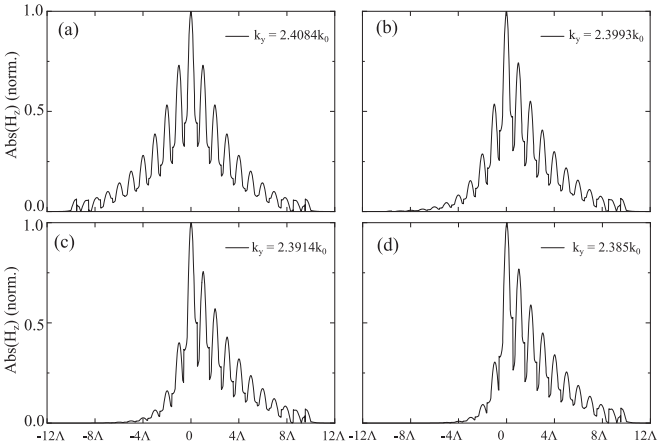

FIG. 10. H_z distributions of the topological interface states for the BA-type connection with ten periods at $\lambda = 1450$ nm from full-wave simulation. The crystals have $d_0 = 52$ nm and $d_a = 10$ nm for the right type-A lattices. The left type-B lattices have (a) $d_a = -10$ nm, (b) $d_a = -20$ nm, (c) $d_a = -30$ nm, and (d) $d_a = -40$ nm.

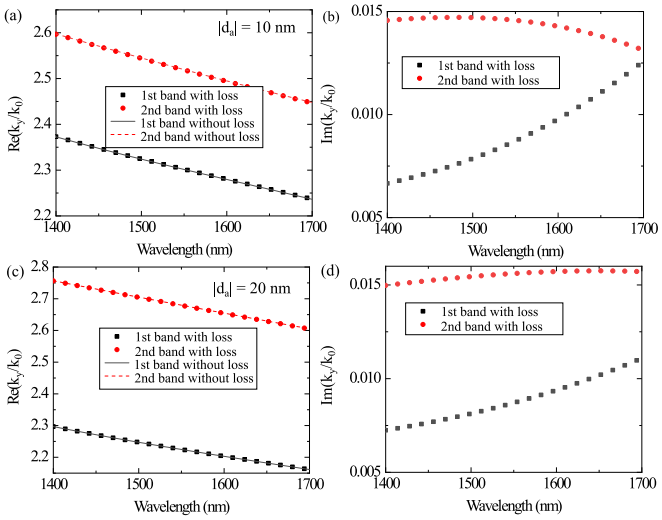

FIG. 11. The band structure for this 1D crystal with $q = 0$ obtained by Eq. (1). The geometrical parameters of the lattice for (a), (b) are same as that in Fig. 2(b), i.e., $d_0 = 52$ nm and $|d_a| = 10$ nm, and the same for (c), (d) is with $d_0 = 52$ nm and $|d_a| = 20$ nm.

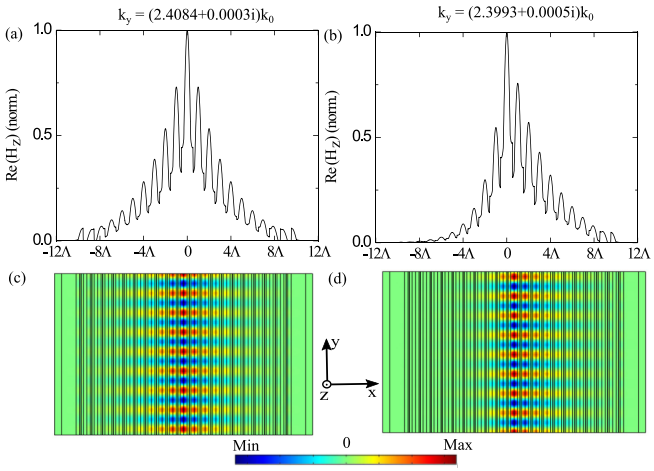

FIG. 12. The field distribution of magnetic component H_z for the BA-type connection. The geometrical structure for the left panel is the same as that in Fig. 10(a), and the right panel is the same as that in Fig. 10(b).

lattices via a full-wave simulation using the finite element method. Figure 10 shows the H_z distributions of the topological interface states predicted by the intersection points (black dots) in Fig. 2(c).

APPENDIX E: LOSS EFFECT ON THE DISPERSION RELATION AND THE EXISTENCE OF INTERFACE STATES

In our considered frequency region, the loss of silver is relatively small compared to the real part. For example, the relative permittivity for the wavelength 1550 nm is $\varepsilon_2 = -125.179 + 2.888i$. Now we focus the effect of the loss on the dispersion relation. Here, we take the case of Fig. 2(b) as an example. If the loss of metal is added, the bands structures for $q = 0$ are shown in Fig. 11. It is obvious that the loss factor can barely affect the real parts of k_y, and the corresponding imaginary parts are completely small.

To investigate the propagation of the interface states on the condition that loss of metal is involved, we take the wavelength of $\lambda = 1450$ nm and the BA-type connection (as revealed in Fig. 10) as an example. In our model, the loss cannot smear out the gap of the inversion-symmetry-breaking crystal, as illustrated in Fig. 11. Thus the prediction based on the Hermitian case is still valid. Figure 12 clearly shows the existence of the interface states for the BA-type connection and their propagation with little attenuation. By contrast to the results in Fig. 10 of the main text, the off-axis k_y are consistent except for the small attenuation.

[1] M. Z. Hasan and C. L. Kane, Rev. Mod. Phys. **82**, 3045 (2010).
[2] X.-L. Qi and S.-C. Zhang, Rev. Mod. Phys. **83**, 1057 (2011).
[3] B. A. Bernevig and T. L. Hughes, *Topological Insulators and Topological Superconductors* (Princeton University Press, Princeton, NJ, 2013).
[4] L. Fu and C. L. Kane, Phys. Rev. B **76**, 045302 (2007).
[5] A. P. Schnyder, S. Ryu, A. Furusaki, and A. W. W. Ludwig, Phys. Rev. B **78**, 195125 (2008).
[6] A. B. Khanikaev, S. H. Mousavi, W.-K. Tse, M. Kargarian, A. H. MacDonald, and G. Shvets, Nat. Mater. **12**, 233 (2013).
[7] J. Lu, C. Qiu, S. Xu, Y. Ye, M. Ke, and Z. Liu, Phys. Rev. B **89**, 134302 (2014).
[8] P. Tang, Q. Zhou, G. Xu, and S.-C. Zhang, Nat. Phys. **12**, 1100 (2016).
[9] G. G. Pyrialakos, N. S. Nye, N. V. Kantartzis, and D. N. Christodoulides, Phys. Rev. Lett. **119**, 113901 (2017).
[10] M. Yan, H. Huang, K. Zhang, E. Wang, W. Yao, K. Deng, G. Wan, H. Zhang, M. Arita, H. Yang, Z. Sun, H. Yao, Y. Wu, S. Fan, W. Duan, and S. Zhou, Nat. Commun. **8**, 257 (2017).
[11] Z. Yan and Z. Wang, Phys. Rev. Lett. **117**, 087402 (2016).
[12] A. A. Soluyanov, D. Gresch, Z. Wang, Q. Wu, M. Troyer, X. Dai, and B. A. Bernevig, Nature **527**, 495 (2015).
[13] S. Jia, S.-Y. Xu, and M. Z. Hasan, Nat. Mater. **15**, 1140 (2016).
[14] C. He, X. Ni, H. Ge, X.-C. Sun, Y.-B. Chen, M.-H. Lu, X.-P. Liu, and Y.-F. Chen, Nat. Phys. **12**, 1124 (2016).
[15] Z. Yang and B. Zhang, Phys. Rev. Lett. **117**, 224301 (2016).
[16] M. S. Rudner, N. H. Lindner, E. Berg, and M. Levin, Phys. Rev. X **3**, 031005 (2013).
[17] B. Bradlyn, J. Cano, Z. Wang, M. G. Vergniory, C. Felser, R. J. Cava, and B. A. Bernevig, Science **353**, aaf5037 (2016).
[18] A. V. Nalitov, G. Malpuech, H. Terças, and D. D. Solnyshkov, Phys. Rev. Lett. **114**, 026803 (2015).
[19] V. G. Sala, D. D. Solnyshkov, I. Carusotto, T. Jacqmin, A. Lemaître, H. Terças, A. Nalitov, M. Abbarchi, E. Galopin, I. Sagnes, J. Bloch, G. Malpuech, and A. Amo, Phys. Rev. X **5**, 011034 (2015).

[20] A. V. Nalitov, D. D. Solnyshkov, and G. Malpuech, Phys. Rev. Lett. **114**, 116401 (2015).
[21] M. Milićević, G. Montambaux, T. Ozawa, I. Sagnes, A. Lemaître, L. L. Gratiet, A. Harouri, J. Bloch, and A. Amo, arXiv:1807.08650.
[22] C.-R. Mann, T. J. Sturges, G. Weick, W. L. Barnes, and E. Mariani, Nat. Commun. **9**, 2194 (2018).
[23] H.-X. Wang, Y. Chen, Z. H. Hang, H.-Y. Kee, and J.-H. Jiang, npj Quantum Mater. **2**, 54 (2017).
[24] C. Hu, Z. Li, R. Tong, X. Wu, Z. Xia, L. Wang, S. Li, Y. Huang, S. Wang, B. Hou, C. T. Chan, and W. Wen, Phys. Rev. Lett. **121**, 024301 (2018).
[25] S. Raghu and F. D. M. Haldane, Phys. Rev. A **78**, 033834 (2008).
[26] F. D. M. Haldane and S. Raghu, Phys. Rev. Lett. **100**, 013904 (2008).
[27] Z. Wang, Y. D. Chong, J. D. Joannopoulos, and M. Soljačić, Phys. Rev. Lett. **100**, 013905 (2008).
[28] Z. Wang, Y. Chong, J. D. Joannopoulos, and M. Soljačić, Nature **461**, 772 (2009).
[29] L.-H. Wu and X. Hu, Phys. Rev. Lett. **114**, 223901 (2015).
[30] Y. Yang, Y. F. Xu, T. Xu, H.-X. Wang, J.-H. Jiang, X. Hu, and Z. H. Hang, Phys. Rev. Lett. **120**, 217401 (2018).
[31] J.-W. Dong, X.-D. Chen, H. Zhu, Y. Wang, and X. Zhang, Nat. Mater. **16**, 298 (2017).
[32] X. Wu, Y. Meng, J. Tian, Y. Huang, H. Xiang, D. Han, and W. Wen, Nat. Commun. **8**, 1304 (2017).
[33] J. Noh, S. Huang, K. P. Chen, and M. C. Rechtsman, Phys. Rev. Lett. **120**, 063902 (2018).
[34] M. Xiao, Z. Q. Zhang, and C. T. Chan, Phys. Rev. X **4**, 021017 (2014).
[35] X. Huang, M. Xiao, Z.-Q. Zhang, and C. T. Chan, Phys. Rev. B **90**, 075423 (2014).
[36] For silver, the relative permittivity is $\varepsilon_2 = \varepsilon_\infty - \omega_p^2/\omega(\omega + i\gamma)$ with $\varepsilon_\infty = 3.7$, $\omega_p = 1.38 \times 10^{16}\,\mathrm{rad\,s^{-1}}$, and $\gamma = 2.723 \times 10^{13}\,\mathrm{rad\,s^{-1}}$.
[37] S. H. Nam, E. Ulin-Avila, G. Bartal, and X. Zhang, Opt. Express **18**, 25627 (2010).
[38] S. H. Nam, A. J. Taylor, and A. Efimov, Opt. Express **18**, 10120 (2010).
[39] A. Yariv and P. Yeh, *Optical Waves in Crystals* (Wiley, New York, 1984).
[40] M. Xiao, G. Ma, Z. Yang, P. Sheng, Z. Q. Zhang, and C. T. Chan, Nat. Phys. **11**, 240 (2015).
[41] A. H. Castro Neto, F. Guinea, N. M. R. Peres, K. S. Novoselov, and A. K. Geim, Rev. Mod. Phys. **81**, 109 (2009).
[42] S. Manzeli, D. Ovchinnikov, D. Pasquier, O. V. Yazyev, and A. Kis, Nat. Rev. Mater. **2**, 17033 (2017).
[43] C. Kumar, S. K. Srivastav, P. Adhikary, S. Banerjee, T. Das, and A. Das, Phys. Rev. B **98**, 155408 (2018).